

# Extraction of neutron density distributions from high-statistics coherent elastic neutrino-nucleus scattering data

D. Aristizabal Sierra<sup>1,\*</sup>

<sup>1</sup>*Universidad Técnica Federico Santa María - Departamento de Física  
Casilla 110-V, Avda. España 1680, Valparaíso, Chile*

Forthcoming fixed-target coherent elastic neutrino-nucleus scattering experiments aim at measurements with  $O(\text{tonne})$ -scale detectors and substantially reduced systematic and statistical uncertainties. With such high quality data, the extraction of point-neutron distributions mean-square radii requires a better understanding of possible theoretical uncertainties. We quantify the impact of single-nucleon electromagnetic mean-square radii on the weak-charge form factor and compare results from weak-charge form factor parametrizations and weak-charge form factor decompositions in terms of elastic vector proton and neutron form factors, including nucleon form factors  $Q$ -dependent terms up to order  $Q^2$ . We assess as well the differences arising from results derived using weak-charge form factor decompositions in terms of elastic vector proton and neutron form factors and a model-independent approach based solely on the assumption of spherically symmetric nuclear ground state. We demonstrate the impact of the main effects by assuming pseudo-data from a one-tonne LAr detector and find that, among the effects and under the assumptions considered in this paper, weak-charge form factor parametrizations and weak-charge form factor decompositions in terms of elastic vector proton and neutron form factors enable the extraction of the  $^{40}\text{Ar}$  point-neutron distribution mean-square radius with a  $\sim 15\%$  accuracy. With a substantial reduction of the beam-related neutron and steady-state backgrounds a  $\sim 1\%$  precision extraction seems feasible, using either of the two approaches.

## CONTENTS

|   |    |
|---|----|
| I. Introduction   | 1  |
| II. Nuclear charge and weak-charge form factors   | 2  |
| A. Electromagnetic and weak charge radii  | 3  |
| III. Theoretical and phenomenological uncertainties   | 3  |
| A. Uncertainties due to leading-order point-proton distribution mean-square radius and leading-order nucleon form factors | 4  |
| B. Uncertainties due to elastic vector proton and neutron form factor parametrizations                                    | 6  |
| C. Model-independent versus form factor parametrizations approaches   | 6  |
| IV. CEvNS cross section and event rate  | 8  |
| V. Extraction of the argon neutron distribution root-mean-square radius using different approaches                        | 10 |
| VI. Conclusions   | 13 |
| Acknowledgments   | 13 |
| References  | 13 |

## I. INTRODUCTION

Since its first observation by the COHERENT collaboration in 2017 [1], CEvNS has become a powerful tool for the

determination of nuclear and SM properties as well as for constraining new physics. Current datasets involve measurements in CsI and LAr detectors with fiducial volumes in the order of 10 kg [1–3]. With such active volumes, the datasets comprise about  $\sim 100$  events, with—to a certain degree—sizable systematics and statistical uncertainties. Using these data a wide range of analyses have been carried out. They include the determination of cesium, iodide and argon point-neutron distributions root-mean-square (rms) radii [4–9], measurements of the weak mixing angle at renormalization scales of the order of 50 MeV [5, 6, 9, 10], constraints on new interactions in the neutrino sector [11–24], constraints on neutrino electromagnetic properties [25–27] and limits on sterile neutrinos [10].

Plans for enhancing statistics by deploying an  $O(\text{tonne})$  LAr detector in the future second target station (STS) at the Oak Ridge National Laboratory have been discussed in Refs. [28, 29] (see Ref. [30] as well)<sup>1</sup>. With improvements on statistical and systematic uncertainties, such detector will deliver high quality data with which improvements on the different analyses that have been done so far are expected. This calls for a better understanding of theoretical uncertainties. For instance—depending on the experimental uncertainties—the inclusion of one-loop order electroweak corrections [34] might become necessary, regardless of the physics case the data will be used for.

As far as we know, the extraction of point-neutron distributions mean-square radii with existing or forecasted data has been done considering only leading order (LO) effects. With this in this paper we mean the following: The measured nuclear charge radius and the point-proton distribution rms ra-

<sup>1</sup> The Coherent Captain-Mills Experiment at Los Alamos National Laboratory aims at measurements with an  $O(\text{tonne})$  LAr detector as well [31] (see e.g. Refs. [32, 33] for discussions of its physics reach).

\* daristizabal@ulg.ac.be

dius have been assumed to be equal, and only LO nucleon form factor terms ( $Q$  independent terms) have been considered [6, 35–37]. Furthermore, analyses using nuclear weak-charge form factor parametrizations, nuclear weak-charge form factor decompositions in terms of elastic vector proton and neutron form factors and power series expansions of the nuclear weak-charge form factor have been used [4, 8, 36–38]. With all of them implying—in principle—different precision levels.

In this paper we quantify the uncertainties implied by considering only LO effects—defined as we have done in the previous paragraph—in the extraction of point-neutron distributions mean-square radii. The analysis is split in two parts. In the first part, we quantify uncertainties at the nuclear weak-charge level for heavy and light nuclei (cesium and argon, taken as representative examples of heavy and light nuclei). To do so we compare results from calculations using only LO effects with calculations where: (a) The point-proton distribution radius is corrected with single-nucleon electromagnetic mean-square radii, (b) nucleon form factor  $Q$ -dependent terms (up to order  $Q^2$ ) are included<sup>2</sup>. We then determine the uncertainties implied by the most commonly used form factor parametrizations and by expansions in terms of even moments.

In the second part, we quantify the precision at which the

point-neutron distribution rms radius can be extracted, including the main effects found in the first part. In this case we proceed by assuming pseudo-data from a one-tonne LAr detector with assumptions on the beam-related neutron (BRN) and steady-state (SS) backgrounds as well as systematic uncertainties extrapolated from current COHERENT measurements.

The remainder of this paper is organized as follows. In Sec. II we provide a general discussion of the nuclear charge and weak-charge form factors as well as of the nuclear charge and weak-charge radii. In Sec. III we determine nuclear weak-charge form factor uncertainties, while in Sec. IV we briefly discuss the CEvNS differential cross section and differential event rate. In Sec. V, based on the results from Sec. III, we extract the  $^{40}\text{Ar}$  neutron distribution mean-square radius. Our conclusions are presented in Sec. VI

## II. NUCLEAR CHARGE AND WEAK-CHARGE FORM FACTORS

The single-nucleon electromagnetic and weak currents can be expressed in terms of the Sachs form factors [41]. For a nucleon  $N$  ( $N = n, p$ ) they read

$$J_{\text{EM}}^{\mu,N} = \bar{u}^{s'}(p') \left[ G_E^N \gamma^\mu + \left( \frac{G_M^N - G_E^N}{1 + \tau} \right) \left( \tau \gamma^\mu + i \sigma^{\mu\nu} \frac{q_\nu}{2m} \right) \right] u^s(p), \quad (1)$$

$$J_{\text{NC}}^{\mu,N} = \bar{u}^{s'}(p') \left[ \tilde{G}_E^N \gamma^\mu + \left( \frac{\tilde{G}_M^N - \tilde{G}_E^N}{1 + \tau} \right) \left( \tau \gamma^\mu + i \sigma^{\mu\nu} \frac{q_\nu}{2m} \right) \right] u^s(p). \quad (2)$$

where  $m$  is a universal nucleon mass,  $q = p' - p$  the transferred four momentum and  $\tau = Q^2/4/m^2$  (with  $Q^2 = -q^2$  a timelike vector) and  $u^s(p)$  and  $u^{s'}(p')$  on-shell nucleon spinors.  $G_{E,M}^N = G_{E,M}^N(Q^2)$  and  $\tilde{G}_{E,M}^N = \tilde{G}_{E,M}^N(Q^2)$  are the single-nucleon form factors for  $N$ . The weak neutral current (NC) involves as well axial and pseudoscalar form factors, which are sensitive to the nucleon spin distribution in the nuclear medium. For elastic scattering their contribution can then be regarded as a subleading effect (actually vanishing in nuclei with even number of protons and neutrons), and so are not considered in Eq. (2).

The nuclear charge and weak-charge form factors follow from: (i) Trading the on-shell nucleon spinors to spinor wavefunctions that account for nucleons in a potential, (ii) assuming the impulse approximation (i.e. assuming that single-nucleon form factors are valid as well in the nuclear medium), (iii) integration over nuclear volume, (iv) taking into account contributions from protons and neutrons (for details see e.g.

[40]). Explicitly one finds

$$ZF_C = \sum_{N=p,n} \left\{ G_E^N F_V^N + \left( \frac{G_M^N - G_E^N}{1 + \tau} \right) \left( \tau F_V^N + \frac{q}{2m} F_T^N \right) \right\}, \quad (3)$$

$$Q_W F_W = \sum_{N=p,n} \left\{ \tilde{G}_E^N F_V^N + \left( \frac{\tilde{G}_M^N - \tilde{G}_E^N}{1 + \tau} \right) \left[ \tau F_V^N + \frac{q}{2m} F_T^N \right] \right\}, \quad (4)$$

with  $Q_W$  determined by the couplings of the proton and neutron to the  $Z$  gauge boson,  $Q_W = N g_V^n + Z g_V^p$  ( $g_V^p = 1/2 - 2 \sin^2 \theta_W$  and  $g_V^n = -1/2$ )<sup>3</sup>. Note that the form factors written as in Eqs. (3) and (4) satisfy the normalization condition  $F_C(Q^2 = 0) = F_W(Q^2 = 0) = 1$ . These expressions contain information on nucleon and nuclear structure, the latter encoded in the vector and tensor nuclear form factors. Spin-orbit effects governed by  $F_T$  are subleading compared with nuclear

<sup>2</sup> Other subleading effects involve as well relativistic Darwin-Foldy and spin-orbit corrections [39, 40], which our analysis does not account for.

<sup>3</sup> One-loop corrected proton and neutron electroweak couplings are given by  $g_V^p = 0.0721$  and  $g_V^n = -0.988$  [42]. These are the values we use in the calculations presented in Secs. III and V.

spin-independent effects controlled by  $F_V$  [40]. Thus keeping only LO effects and taking into account that  $\tau \ll 1$  for the typical transferred momentum in neutrino stopped-pion sources ( $Q^2 \lesssim m_\pi^2/2$ ), the charge and weak-charge form factors reduce to a rather simple form

$$F_C(q^2) = \frac{1}{Z} [G_E^p(q^2)F_V^p(q^2) + G_E^n(q^2)F_V^n(q^2)], \quad (5)$$

$$F_W(q^2) = \frac{1}{Q_W} [\tilde{G}_E^p(q^2)F_V^p(q^2) + \tilde{G}_E^n(q^2)F_V^n(q^2)]. \quad (6)$$

Numerically one finds that spin-orbit effects are of the order of 0.1% [40], while terms proportional to  $\tau$  contribute at the order of 0.01% in stopped-pion neutrino experiments where  $Q^2 \simeq (10\text{MeV})^2$ . Eqs. (5) and (6) are thus precise enough at the percent level.

### A. Electromagnetic and weak charge radii

LO expressions for the electromagnetic and weak-charge radii of the nucleus follow from Eqs. (5) and (6), as we now discuss. Assuming spherical symmetry, the nucleon and spin-independent nucleon structure functions can be expanded in terms of their moments. For nucleons one has

$$G_E^{p,n} = \sum_{i=0,1}^{\infty} (-1)^i \frac{Q^{2i}}{(2i+1)!} r_X^{2i}, \quad (7)$$

$$\tilde{G}_E^X = g_V^X \sum_{i=0}^{\infty} (-1)^i \frac{Q^{2i}}{(2i+1)!} \tilde{r}_X^{2i}, \quad (8)$$

where the order  $Q^2$  terms in the expansion in Eq. (7) involve the single-nucleon electromagnetic mean-square radii,  $r_X^2$  ( $X = p, n$ ), while those in Eq. (8) the single-nucleon weak-charge mean-square radii,  $\tilde{r}_X^2$ . In Eq. (7) the sum starts at  $i = 0$  ( $i = 1$ ) for protons (neutrons). For the spin-independent nuclear form factors one instead has (see e.g. [38])

$$F_V^p = Z \sum_{i=0}^{\infty} (-1)^i \frac{Q^{2i}}{(2i+1)!} R_p^{2i}, \quad (9)$$

$$F_V^n = N \sum_{i=0}^{\infty} (-1)^i \frac{Q^{2i}}{(2i+1)!} R_n^{2i}. \quad (10)$$

In this case—at order  $Q^2$ —terms involve the point-proton and point-neutron distributions mean-square radii,  $R_p^2$  and  $R_n^2$  (second moment of the distributions)<sup>4</sup>. The nuclear charge and weak-charge radii,  $R_C^2$  and  $R_W^2$ , follow from

$$R_C^2 = -6 \left. \frac{dF_C}{dQ^2} \right|_{Q^2=0}, \quad R_W^2 = -6 \left. \frac{dF_W}{dQ^2} \right|_{Q^2=0}, \quad (11)$$

after expansions in Eqs. (7), (8), (9) and (10) are inserted in Eqs. (5) and (6). Their explicit expressions are given by

$$R_C^2 = R_p^2 + r_p^2 + \frac{N}{Z} r_n^2, \quad (12)$$

$$R_W^2 = \frac{Z g_V^p}{Q_W} (R_p^2 + \tilde{r}_p^2) + \frac{N g_V^n}{Q_W} (R_n^2 + \tilde{r}_n^2). \quad (13)$$

The single-nucleon weak-charge mean-square radii in  $R_W$  can be reexpressed in terms of the single-nucleon electromagnetic mean-square radii as follows [40]

$$\tilde{r}_p^2 = r_p^2 + \frac{g_V^n}{g_V^p} r_n^2 + \xi_V^{(0)} r_s^2, \quad \tilde{r}_n^2 = r_p^2 + \frac{g_V^p}{g_V^n} r_n^2 + \xi_V^{(0)} r_s^2, \quad (14)$$

where  $\xi_V^{(0)} = g_V^u + g_V^d + g_V^s$  (with  $g_V^q$  the quark  $q$  weak-vector charge) and  $r_s^2$  the mean-square strange radius. Numerically,  $\xi_V^{(0)} = -0.988$  and  $r_s^2 = -0.00430 \text{ fm}^2$  with the latter obtained from lattice QCD calculations [43]. Thus, the strange quark contribution provides per mille corrections to the proton and neutron LO expressions in Eq. (14). It can therefore be neglected in the following analysis.

With the aid of these equations the weak-charge mean-square radius can finally be rewritten as

$$R_W^2 = \frac{Z}{Q_W} (g_V^p R_p^2 + g_V^p r_p^2 + g_V^n r_n^2) + \frac{N}{Q_W} (g_V^n R_n^2 + g_V^n r_p^2 + g_V^p r_n^2), \quad (15)$$

which in turn can be recast in terms of the electromagnetic charge radius and the neutron skin,  $R_n^2 - R_p^2$ , [8]

$$R_W^2 = R_C^2 + \frac{N g_V^n}{Q_W} \left[ (R_n^2 - R_p^2) + \frac{Z^2 - N^2}{NZ} r_n^2 \right]. \quad (16)$$

Due to the small transferred momentum, stopped-pion CEvNS experiments are not particularly sensitive to nucleon structure. Thus the nucleon form factors in Eqs. (5) and (6) can be truncated at order  $Q^2$ , resulting in the following expression for the weak-charge form factor [8]

$$F_W \simeq \frac{1}{Q_W} \left[ Z \left( g_V^p - \frac{g_V^p}{6} r_p^2 Q^2 - \frac{g_V^n}{6} r_n^2 Q^2 \right) F_V^p(Q^2) + N \left( g_V^n - \frac{g_V^n}{6} r_p^2 Q^2 - \frac{g_V^p}{6} r_n^2 Q^2 \right) F_V^n(Q^2) \right], \quad (17)$$

where the nuclear form factors have been normalized,  $F_V^p(Q^2 = 0) = 1$  and  $F_V^n(Q^2 = 0) = 1$ .

### III. THEORETICAL AND PHENOMENOLOGICAL UNCERTAINTIES

In this Section we determine the numerical variations to which the weak-charge form factor can be subject to. For that aim we consider the Helm parametrization [44] for the elastic vector proton and neutron form factors (see Sec. III A). We

<sup>4</sup> Here following standard conventions we use lower-case for nucleons and upper-case for nuclei.

first quantify  $F_W$  by considering LO expressions for the point-proton distribution mean-square radius and the nucleon form factors, which we compare with  $F_W$  obtained by considering the full expression in Eq. (17), including the single-nucleon electromagnetic mean-square radii in the determination of  $R_p$ . We compare as well those results with those obtained assuming the Helm parametrization for the weak-charge form factor. We then proceed to calculate  $F_W$  by assuming different parametrizations for the elastic vector proton and neutron nuclear form factors. Our analysis relies on the Fourier transform of the symmetrized Fermi function [39] and the Klein-Nystrand [45] parametrizations, in addition to the Helm approach. In doing so, we quantify the dependence of  $F_W$  on parametrization choice. Finally, we compare the parametrization approach with the model-independent treatment based on series expansions of the elastic vector proton and neutron form factors.

### A. Uncertainties due to leading-order point-proton distribution mean-square radius and leading-order nucleon form factors

We start by considering three different cases, two limits and the full case:

- 1) **Limit 1 (Case 1):** LO nucleon form factors ( $Q$ -independent terms) and point-proton distribution mean-square radius equal to the nuclear charge mean-square radius,  $R_p^2 = R_C^2$ .
- 2) **Limit 2 (Case 2):** LO nucleon form factors and full point-proton distribution mean-square radius given by Eq. (12).
- 3) **Full case (Case 3):** Full nucleon form factors, up to  $Q^2$  as given in Eq. (17) and full point-proton distribution mean-square radius given by Eq. (12).

These limits are motivated as follows. In most analyses in which the point-neutron distribution rms radius is extracted from CEvNS data (see e.g. Ref. [37]) the point-proton distribution mean-square radius is fixed to be equal to the nuclear charge radius. As can be seen from Eq. (12), doing so overestimates  $R_p$ . A larger value for  $R_p$  means a smaller value for  $F_p$  at a given  $Q$ . Under such simplification, an uncertainty in the extraction of  $R_n^2$  from CEvNS data is implied. Order  $Q^2$  corrections in the nucleon form factors are also typically ignored and, though suppressed, are potentially a source of sizable uncertainties. Ignoring order  $Q^2$  terms enhance  $F_W$  [see Eq. (17)], and so the CEvNS event rate, resulting in a potential underestimation of  $R_n^2$ .

To proceed, we adopt the Helm form factor parametrization for the elastic vector proton and neutron form factors,  $F_V^p$  and  $F_V^n$ , namely [44]

$$F_H(Q^2) = 3 \frac{j_1(QR_0)}{QR_0} e^{-(Qs)^2/2}. \quad (18)$$

Here  $R_0$  refers to the diffraction radius, related with the point-nucleon distribution mean-square radius through the skin

thickness  $s = 0.9$  fm [46] according to

$$R_0 = \sqrt{\frac{5}{3} (R_X^2 - 3s^2)} \quad (X = p, n). \quad (19)$$

To avoid mixing nuclear physics effects with detector effects we use argon and cesium as target materials. For argon this means one can assume the detector to be 100% composed of  $^{40}\text{Ar}$  (up to per mille corrections), while for cesium of  $^{133}\text{Cs}$ . Parameters used in our calculation are displayed in Tab. I, along with the values for the single-nucleon electromagnetic mean-square radii central values [47].

|                            |                  |                   |
|----------------------------|------------------|-------------------|
| Isotope                    | $^{40}\text{Ar}$ | $^{133}\text{Cs}$ |
| Abundance ( $X_i$ )        | 99.6%            | 100.0%            |
| $R_C$ [fm]                 | 3.4274           | 4.0414            |
| Nucleon                    | Proton           | Neutron           |
| $r_X^2$ [fm <sup>2</sup> ] | 0.7071           | -0.1155           |

TABLE I.  $^{40}\text{Ar}$  and  $^{133}\text{Cs}$  relative abundances along with their nuclear charge radii used in our calculation. Nuclear charge radii taken from Ref. [48]. Single-nucleon electromagnetic mean-square radii central values taken from Ref. [47].

To quantify deviations implied by the limits in items 1 and 2 with the full result in item 3 the following percentage difference factor is employed

$$\Delta F_W [\%] = \frac{F_W|_{C_i} - F_W|_{C_j}}{F_W|_{C_i}} \times 100\%, \quad (20)$$

where  $F_W|_{C_i} > F_W|_{C_j}$  and  $C_{i,j}$  refer to the cases used for the calculation of the weak-charge form factor. The results are shown in Fig. 1. We have fixed the point-neutron distribution rms radius according to  $R_n = R_p + 0.1$  fm and  $R_n = R_p + 0.2$  fm for argon and cesium, respectively. Note that these choices are not intended to represent the actual values. They are rather used as proxies whose motivation is that of covering values predicted by different theoretical nuclear methods [36]. Results following from this choice are rather stable provided  $R_n$  does not largely differs from  $R_p$ , somehow expected for the nuclei we are interested in.

From Fig. 1 (left graph) one can see that by assuming that the point-proton rms radius distribution amounts to the measured nuclear charge rms radius has a small effect. All over the relevant transferred momentum range ( $Q^2 \lesssim m_\mu^2$ ) deviations are at (or below) the per mille level, regardless of nuclide. Including the single-nucleon electromagnetic mean-square radii in the determination of  $R_p^2$  becomes relevant only if experimental uncertainties reach that level of precision, otherwise the  $R_p^2 = R_C^2$  approximation is fairly accurate. Differences due to nucleon form factors  $Q$ -dependent terms are instead slightly more relevant. Results in Fig. 1 (right graph) show that they can reach values up to 3%, basically regardless of nuclide. Nucleon form factors effects should then accounted for in high-statistics CEvNS experiments with low systematic and statistical uncertainties.

Rather than calculating the weak-charge form factor using Eq. (17), one could instead use a form factor parametrization

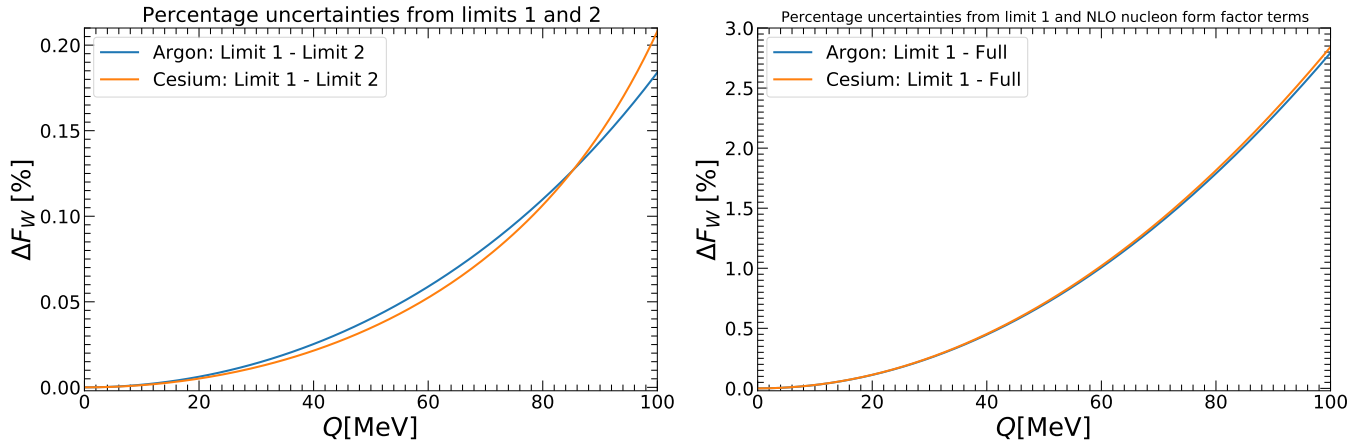


FIG. 1. Nuclear weak-charge form factor percentage difference calculated according to Eq. (20) and for: Nucleon form factors LO terms (momentum-independent terms only) and  $R_p^2 = R_C^2$  (**Limit 1**, item 1), nucleon form factor LO terms and  $R_p^2 = R_C^2 - r_p^2 - (N/Z)r_n^2$  (**Limit 2**, item 2), full nucleon form factors up to order  $Q^2$  (**Full**, item 3) and  $R_p^2 = R_C^2 - r_p^2 - (N/Z)r_n^2$ . **Left graph**: Percentage difference obtained by comparing limits 1 and 2, **Right graph**: percentage difference obtained by comparing limit 1 with full nucleon form factor expressions and  $R_p^2 = R_C^2 - r_p^2 - (N/Z)r_n^2$ . For the point-neutron distribution rms radii we have taken  $R_n = R_p + 0.1$  fm and  $R_n = R_p + 0.2$  fm for argon and cesium, respectively. These values taken just for the sake of illustrating the deviations implied by the different limits compared with the case in which full expressions are considered. For the  $Q$  range displayed in the graphs the neutrino flux is sizable (see text for more details).

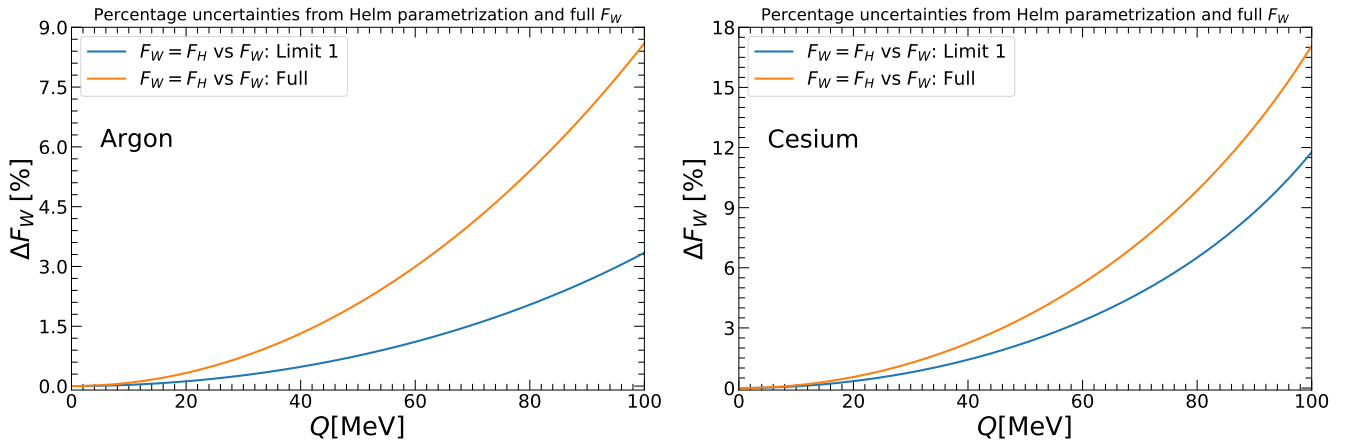


FIG. 2. Nuclear weak-charge form factor percentage uncertainty for argon (left graph) and cesium (right graph) calculated using the Helm parametrization with the diffraction radius  $R_0$  fixed through the weak-charge mean-square radius  $R_W^2$  and by using Eq. (17). Percentage uncertainties are calculated in limit 1 (item 1) and in the full case (item 3). The point-neutron distribution rms radii have been fixed according to  $R_n = R_p + 0.1$  fm and  $R_n = R_p + 0.2$  fm. For the  $Q$  range displayed in the graphs the neutrino flux is sizable (see text for more details).

for  $F_W$ —e.g. the Helm parametrization—and fix  $R_X^2 = R_W^2$  in Eq. (19), with  $R_W^2$  as given in Eq. (16) (as done e.g. in Ref. [8]). Since  $R_W^2$  involves the point-neutron distribution mean-square radius, from such procedure one could as well extract from CEvNS data a range for its value at a certain confidence level. To show what are the expected percentage differences following this procedure with that dictated by Eq. (17), we have calculated  $F_W$  as we have described above and compared with  $F_W$  calculated using Eq. (17) in limit 1 (item 1) and in the full case (item 3). Deviations are quantified with the aid of Eq. (20) where in this case  $C_i$  refers to  $F_W$  calculated through the Helm parametrization and  $C_j$  to  $F_W$  calculated using Eq. (17) in the aforementioned cases.

The result is displayed in Fig. 2, left (right) graph for argon (cesium). One can see that differences between both approaches are more pronounced for heavier nuclei. And grow depending on whether one considers the most simplified assumptions (limit 1) or the full weak-charge form factor including nucleon form factors corrections and single-nucleon electromagnetic mean-square radii. For argon, the percentage uncertainty can raise up to  $\sim 9\%$  while for cesium—instead—up to  $\sim 18\%$ . Some caution, however, is required. Differences grow with transferred momentum and so at their peak (in the relevant range) the stopped-pion neutrino flux is expected to be fading away. Because of kinetic reasons, the contribution of  $\nu_e$  to the delayed component fades away at  $E_\nu = m_\mu/2$ .

The contribution of  $\bar{v}_\mu$  has a sharp fall there as well, but contributes sizably at energies close to the kinematic cut. Thus, evaluating  $E_r^{\max}$  at  $E_\nu = m_\mu/2$  and calculating with that value  $Q_{\max}$  for argon and cesium one finds  $Q_{\max}^{\text{Cs}} \simeq 100\text{MeV}$  and  $Q_{\max}^{\text{Ar}} \simeq 190\text{MeV}$ . It is for this reason that we have plotted only up to  $Q = 100\text{MeV}$ . To assure that deviations are shown in the region where they play a role at the event rate level.

## B. Uncertainties due to elastic vector proton and neutron form factor parametrizations

Event rate spectra derived from form factor parametrizations are expected to depend on the parametrization used, with the dependence increasing with increased  $Q$  [36]. To determine the size of these dependences we calculate  $F_V^p$  and  $F_V^n$  using as well the Klein-Nystrand form factor [45] and the Fourier transform of the symmetrized Fermi distribution [39].

The Klein-Nystrand form factor follows from folding a Yukawa potential (range  $a_k$ ) over a hard sphere distribution of radius  $R_A$ , namely [45]

$$F_{\text{KN}} = 3 \frac{j_1(QR_A)}{QR_A} \frac{1}{1 + Q^2 a_k^2}. \quad (21)$$

The range of the potential  $a_k$  is 0.7 fm [45] and the hard sphere radius is determined through the point-proton and point-neutron distributions mean-square radii according to

$$R_A = \sqrt{\frac{5}{3} (R_X^2 - 6a_k^2)} \quad (X = p, n). \quad (22)$$

The Fourier transform of the symmetrized Fermi distribution follows instead from  $f_{\text{SF}} = f_{\text{F}}(r) + f_{\text{F}}(-r) - 1$ , where  $f_{\text{F}}(r)$  is the conventional Fermi function

$$f_{\text{F}} = \frac{1}{1 + e^{(r-c)/a}}, \quad (23)$$

where  $c$  refers to the half-density radius and  $a$  ( $a = 0.52\text{fm}$  [49]) to the surface diffuseness. The Fourier transform can be analytically integrated resulting in

$$F_{\text{SF}} = \frac{3}{Qc} \left[ \frac{\sin(Qc)}{(Qc)^2} \left( \frac{\pi Qa}{\tanh(\pi Qa)} \right) - \frac{\cos(Qc)}{Qc} \right] \times \left( \frac{\pi Qa}{\sinh(\pi Qa)} \right) \frac{1}{1 + (\pi a/c)^2}. \quad (24)$$

In this case the half-density radius  $c$  proceeds from the point-proton and point-neutron distributions mean-square radii and the surface diffuseness  $a$

$$c = \sqrt{\frac{5}{3} R_X^2 - \frac{7}{3} (\pi a)^2} \quad (X = p, n). \quad (25)$$

We now calculate the weak-charge form factor percentage difference (as a ‘‘measure’’ of the percentage spread implied by parametrization choice) obtained by calculating  $F_W$  according to Eq. (17), using for the elastic vector proton and neutron form factors the three different parametrizations already

discussed. The result is displayed in Fig. 3. The left graph shows results for argon, while the right graph results for cesium. Differences are slightly more pronounced for the latter, thus demonstrating they are more relevant for heavy nuclides. As  $Q$  increases, the Helm form factor decreases more steeply. This effect is less pronounced for the Fourier transform of the symmetrized Fermi distribution and even less for the Klein-Nystrand parametrization. This means that event rates calculated with the Helm form factor will produce slightly less events than those calculated with the Fermi parametrization, and even less than those obtained with the Klein-Nystrand form factor. This translates into percentage differences of the order of 1% (or below) for argon and 2% (or below) for cesium. In summary, percentage differences due to form factor parametrizations of the elastic vector proton and neutron form factors are comparable to those implied by the  $Q$ -dependent nucleon form factor terms discussed in the previous Section.

## C. Model-independent versus form factor parametrizations approaches

Assuming the nucleon distributions to be spherically symmetric (i.e. assuming that the charge density distribution depends solely on the distribution radius) leads to the series expansions of the elastic vector proton and neutron form factors, Eqs. (9) and (10). These expansions, subject only to the spherical symmetry hypothesis, involve the point-nucleon mean-square radii (second radial moment) at order  $Q^2$ . So rather than sticking to a form factor parametrization or a nuclear physics model one can use these expansions to fit  $R_n^2$  to data [38, 50]. The question is of course whether a  $Q^2$ -order description suffices, or whether higher order terms should be included to increase convergence. Ref. [38] addressed this question and ended up concluding that order  $Q^4$  terms are required (for argon for which the analysis was done). Following this approach, this implies the introduction of a new parameter, the fourth radial moment of the nucleon distributions,  $\langle R_X^4 \rangle$  ( $X = p, n$ )<sup>5</sup>.

To compare the accuracy of the model-independent analysis and the form factor parametrization approach, we first calculate the fourth radial moment for the three parametrizations we are using. We do so by taking into account that the series expansions in Eqs. (9) and (10) can be compared term by term to the Taylor expansions of the  $F_V^p(Q^2)$  and  $F_V^n(Q^2)$  functions. Up to order  $Q^4$  this reduces to

$$R_X^2 = -6 \left. \frac{dF_V^X}{dQ^2} \right|_{Q^2=0} \quad \text{and} \quad \langle R_X^4 \rangle = 60 \left. \frac{d^2 F_V^X}{dQ^4} \right|_{Q^2=0}. \quad (26)$$

More generally, the  $2i$ -th moment can be written according to

$$\langle R_X^{2i} \rangle = (-1)^i \frac{(2i+1)!}{i!} \left. \frac{d^i F_V^X}{dQ^{2i}} \right|_{Q^2=0} \quad (X = p, n). \quad (27)$$

<sup>5</sup> Note that we have simplified our notation for the point-nucleon mean-square radii  $R_X^2 \equiv \langle R_X^2 \rangle$ . For  $\langle R_X^4 \rangle$  we do not do so to avoid confusion.

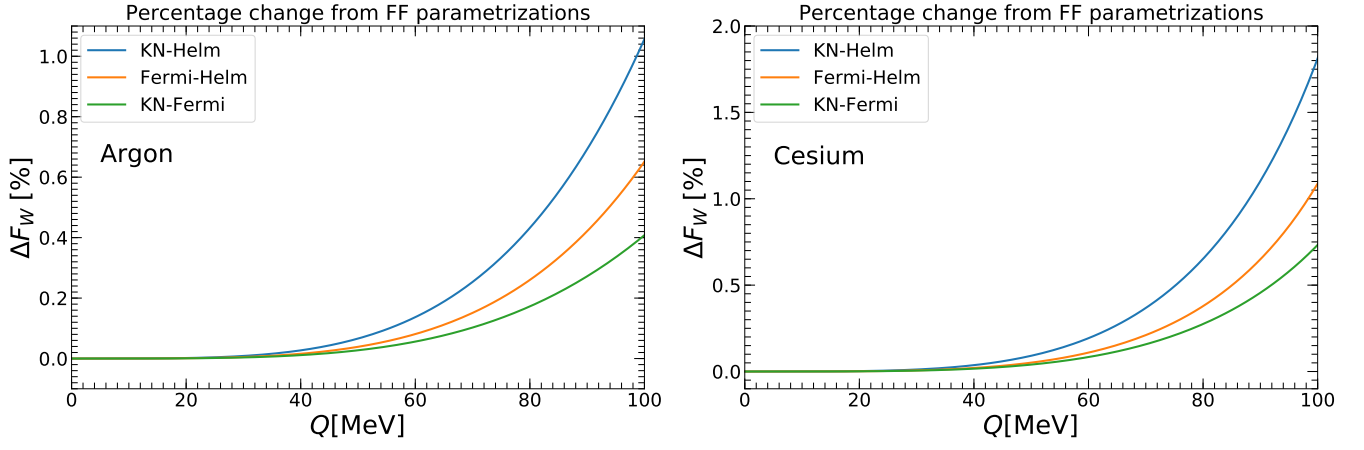


FIG. 3. **Left graph:** Weak-charge form factor percentage difference for argon obtained by using for the elastic vector proton and neutron form factors the Helm, Klein-Nystrand and the Fourier transform of the symmetrized Fermi distribution parametrizations. The results include nucleon form factors  $Q$ -dependent terms (up to order  $Q^2$ ) and single-nucleon electromagnetic mean-square radii. The argon point-neutron distribution rms radius has been fixed according to  $R_n = R_p + 0.1$  fm. **Right graph:** Same as left graph but for cesium, with the point-neutron distribution rms radius fixed according to  $R_n = R_p + 0.2$  fm. For the  $Q$  range displayed in the graphs the neutrino flux is sizable (see text for more details).

The first relation in Eq. (26) leads to the expressions for the diffraction, hard sphere and half density radii ( $R_0$ ,  $R_A$  and  $c$ ) for the Helm, Klein-Nystrand and Fourier transform of the symmetrized Fermi distribution, Eqs. (19), (22) and (25). The second relation in Eq. (26) leads instead to

$$\begin{aligned}
 \text{Helm: } \quad \langle R_X^4 \rangle &= \frac{3}{7}R_0^4 + 6R_0^2s^2 + 15s^4, \\
 \text{KN: } \quad \langle R_X^4 \rangle &= \frac{3}{7}R_A^4 + 12a_k^2R_A^2 + 120a_k^4, \\
 \text{Fermi: } \quad \langle R_X^4 \rangle &= \frac{3}{7}c^4 + \frac{18}{7}c^2(\pi a)^2 + \frac{31}{7}(\pi a)^4. \quad (28)
 \end{aligned}$$

Of course the higher the order in  $Q$  the expansion extends to, the better the convergence and so the reliability of the result. Inclusion of terms up to order  $Q^6$  require the sixth radial moment. From Eq. (27) explicit expressions for each case read

$$\begin{aligned}
 \text{Helm: } \langle R_X^6 \rangle &= \frac{1}{3}R_0^6 + 9R_0^2s^2 + 63R_0^2s^4 + 105s^6, \\
 \text{KN: } \quad \langle R_X^6 \rangle &= \frac{1}{3}R_A^6 + 18R_A^4a_k^2 + 504R_k^2a_k^4 + 5040a_k^6, \\
 \text{Fermi: } \langle R_X^6 \rangle &= \frac{1}{3}c^6 + \frac{11}{3}c^4(\pi a)^2 + \frac{239}{15}c^2(\pi a)^4 + \frac{127}{5}(\pi a)^6. \quad (29)
 \end{aligned}$$

Using Eqs. (19), (22) and (25) for  $R_0$ ,  $R_A$  and  $c$  one can write the fourth and sixth radial moments for each parametrization solely in terms of  $R_X^2$ . In doing so one can then compare the level of convergence of the  $Q^2$ ,  $Q^4$  and  $Q^6$  expansions with the full expressions for each form factor. Results are shown in Figs. 4 and 5 for argon and cesium, respectively (representative of light and heavy nuclides).

Top graphs in Fig. 4 show results for the three form factor parametrizations calculated for argon. Bottom graphs show percentage uncertainties for each case. One can see that inclusion of only the second moment leads to deviations above

$\sim 5\%$  for transferred momenta of the order of 80 MeV. At 100 MeV those deviations can reach  $\sim 20\%$ . These uncertainties, however, should be taken with care as those found in the previous Section for the same reason. They increase at relatively large  $Q$ , where eventually the neutrino flux fades away. Thus, we have plotted up to  $Q$  values where still an abundant number of neutrinos is available. They will—of course—have an impact when comparing results from both approaches, but the best way to understand their actual impact is through the calculation of the CEvNS event rate, something that will be done and discussed in Sec. V.

Top and bottom graphs in Fig. 5 show—instead—results for cesium. In this case a few percentage convergence requires the inclusion of the sixth moment. As can be seen in the bottom graphs, up to order  $Q^4$  the expansion involves uncertainties that can readily reach  $\sim 10\%$  at transferred momenta of the order of 80 MeV, values for which the neutrino flux is still sizable enough for the uncertainty to have an impact on the CEvNS event rate. Aiming at few percent level precision thus requires the inclusion of the sixth moment, inline with Ref. [38].

The adoption of form factor parametrizations suffers from the model dependence implied by the different assumptions those parametrizations come along with. However, as we have discussed in Sec. III B, using one or the other (which can be understood as a variation of the underlying nuclear physics hypotheses) introduces uncertainties at the few percent level. The same level of precision can be achieved with the model-independent power expansion approach, which relies only on the assumption of a spherical symmetric nuclear ground state. However to achieve that level of precision new parameters should be considered. Thus, take for instance the case of cesium. Given a CEvNS dataset an analysis relying on form factor parametrizations is expected to imply a few percent uncertainty (in addition to systematic and statistical

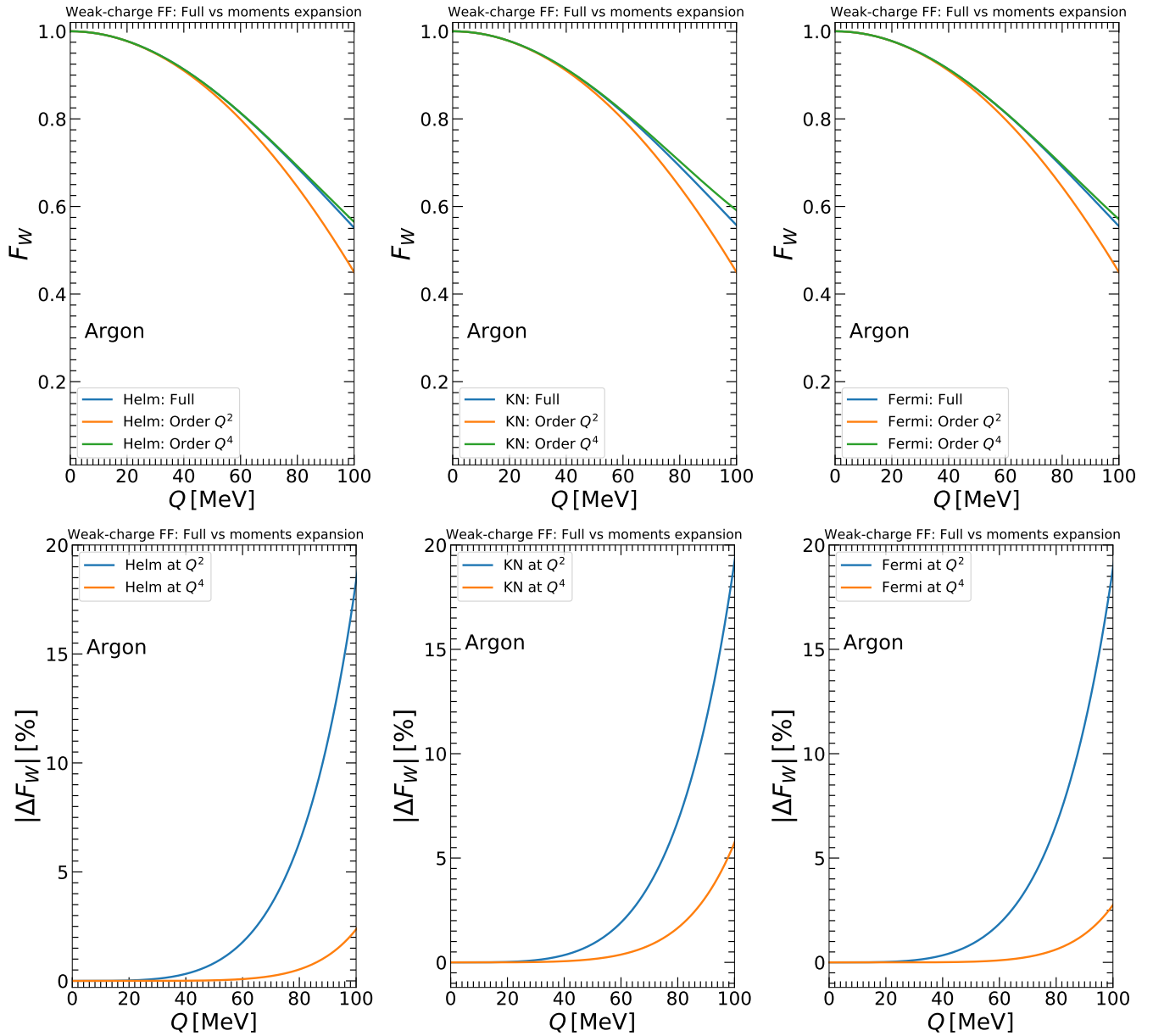


FIG. 4. **Top graphs:** Convergence level for the weak-charge form factor series expansions at order  $Q^2$ ,  $Q^4$  and  $Q^6$  (in argon) for the Helm, Klein-Nystrand and the Fourier transform of the symmetrized Fermi distribution. Expansion at order  $Q^n$  involve radial moments up to  $n$ -th order (see text). **Bottom graphs:** Percentage uncertainty in each case. From these results one can see that if one relies on elastic vector form factor power expansions and demands precision below a few percent the fourth radial moment should be included for light nuclides. In line with Ref. [38]. For the  $Q$  range displayed in the graphs the neutrino flux is sizable (see text for more details).

uncertainties due to e.g. quenching factor, neutrino flux, BRN and SS backgrounds). An analysis based on radial moments expansions as well, but then the dataset has to be used to fit not only the neutron distribution rms radius but also the fourth and sixth moments (depending on the nuclide the detector is built with). The extraction procedure then becomes a multiparameter problem, which might worsen the precision with which  $R_n^2$  can be determined. We will come back to that discussion in Sec. V.

#### IV. CEvNS CROSS SECTION AND EVENT RATE

The CEvNS differential cross section follows from a neutral current process. In terms of nuclear recoil energy it is given by [51–54]

$$\frac{d\sigma}{dE_r} = \frac{G_F^2 m_N}{2\pi} Q_W^2 F_W^2 \left( 2 - \frac{m_N E_r}{E_\nu^2} \right), \quad (30)$$

where subleading kinematic terms have been neglected and  $m_N$  here refers to nuclear mass. The strength at which the



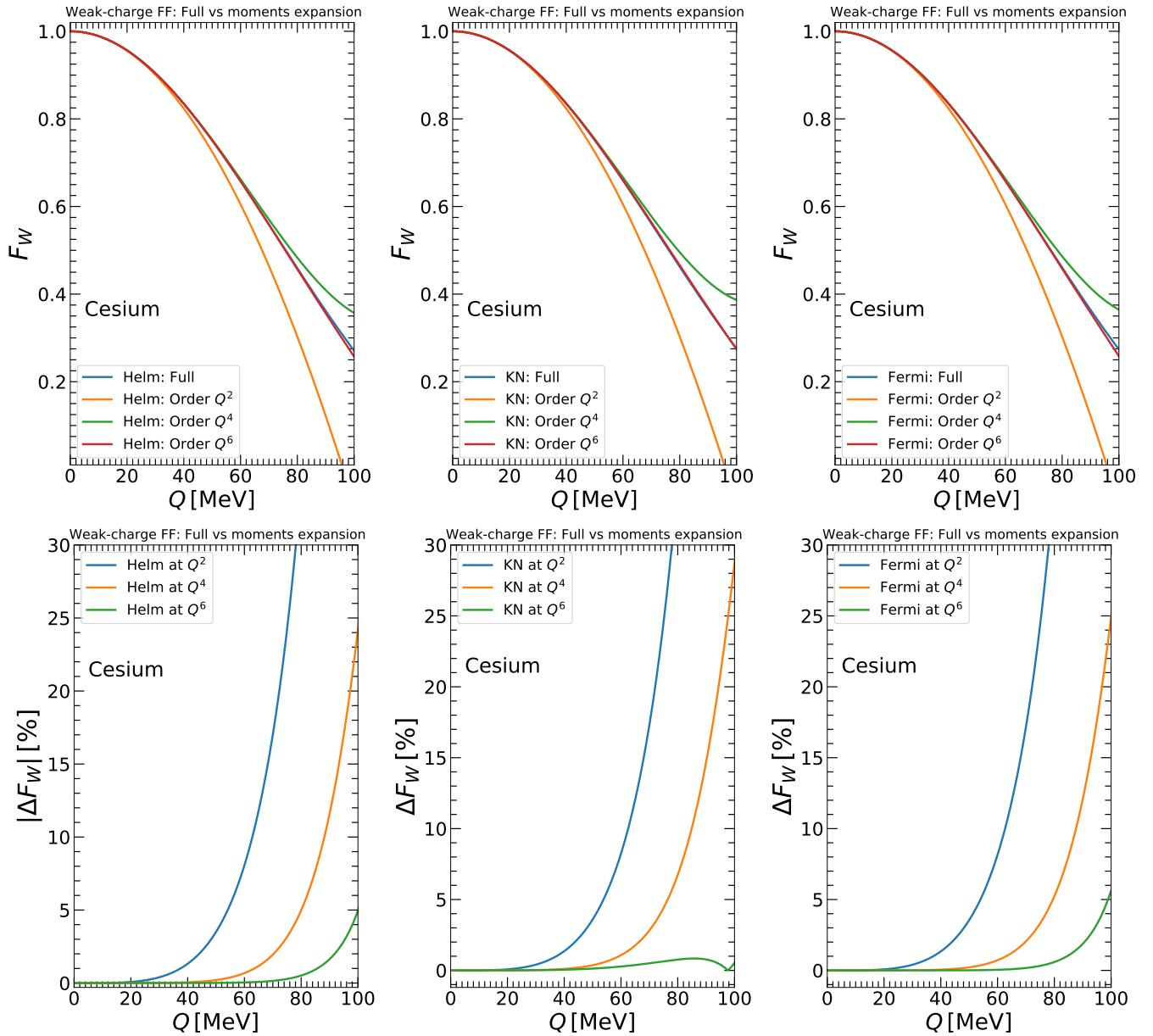


FIG. 5. **Top graphs:** Convergence level for the weak-charge form factor series expansions at order  $Q^2$ ,  $Q^4$  and  $Q^6$  (in cesium) for the Helm, Klein-Nystrand and the Fourier transform of the symmetrized Fermi distribution. Expansion at order  $Q^i$  involve radial moments up to  $n$ -th order (see text). **Bottom graphs:** Percentage uncertainty in each case. From these results one can see that if one relies on elastic vector form factor power expansions and demands precision below a few percent the sixth radial moment should be included. Inline as well with Ref. [38]. For the  $Q$  range displayed in the graphs the neutrino flux is sizable (see text for more details).

$Z$  boson couples to the nucleus is determined by the  $Q$ -dependent coupling  $Q_W \times F_W(Q^2)$ . The coupling is such that with increasing transferred momentum (increasing incoming neutrino energy) the “effective” weak charge decreases and so the interaction probability. Uncertainties in  $F_W$ , as those we have discussed in the previous Sections and as those discussed

in Ref. [36]<sup>6</sup>, translate into uncertainties in the CEvNS cross section. They are indeed responsible for the nuclear physics uncertainties the process involves and so are entirely responsible for the theoretical uncertainties of the CEvNS event rate, unless one-loop electroweak corrections are accounted

<sup>6</sup> Uncertainties on the weak-charge form factor using the large-scale nuclear shell model for a long list of nuclei of interest have been discussed in Ref. [55].

for [34].

The CEvNS differential event rate, as any other rate, follows from a convolution of the differential cross section in Eq. (30) and the incoming neutrino flux. For CEvNS to be used as a tool for the extraction of neutron distributions mean-square radii the neutrino flux should lie in either the “intermediate” or “high” energy windows. The former defined by pion decay at rest, while the latter by pion decay in flight. Note that from this perspective COHERENT experiments operate in the intermediate energy window and the vBDX-DRIFT experiment will in the high energy regime [37, 56]. Because of the large statistics our analysis is interested in we focus on the intermediate energy window, where  $O(\text{tonne})$  detectors are expected in the near future [28, 29]. In this case the neutrino spectrum consist of a monochromatic component (prompt component) and two continuous spectra (delayed components). Their spectral functions follow from the  $\pi^+$  and  $\mu^+$  energy distributions and read

$$\begin{aligned}\Phi_{\nu_\mu} &= \delta\left(E_\nu - \frac{m_\pi^2 - m_\mu^2}{2m_\pi}\right), \\ \Phi_{\bar{\nu}_\mu} &= \frac{192}{m_\mu} \left(\frac{E_\nu}{m_\mu}\right)^2 \left(\frac{1}{2} - \frac{E_\nu}{m_\mu}\right), \\ \Phi_{\nu_e} &= \frac{64}{m_\mu} \left(\frac{E_\nu}{m_\mu}\right)^2 \left(\frac{3}{4} - \frac{E_\nu}{m_\mu}\right).\end{aligned}\quad (31)$$

Since neutrinos are isotropically produced, normalization of the neutrino flux is given by  $n_\nu = r \times \text{POT}/4/\pi^2/L^2$ . We use  $\text{POT} = 2.1 \times 10^{23}/\text{year}$ ,  $L = 28.0$  m and  $r = 8.0 \times 10^{-2}$ , inspired by recent COHERENT measurements and future plans [1–3, 28]. Thus taking into account the three neutrino components, the differential recoil spectrum in a detector with a fiducial volume composed of different stable isotopes is written as

$$\frac{dR}{dE_r} = \frac{m_{\text{det}} N_A}{m_{\text{mol},i}} n_\nu \sum_i X_i \sum_{\alpha=\nu_\mu, \bar{\nu}_\mu, \nu_e} \int_{E_\nu^{\text{min}}}^{E_\nu^{\text{max}}} \Phi_\alpha \frac{d\sigma_i}{dE_r} E_\nu. \quad (32)$$

Here  $m_{\text{det}}$  refers to the detector fiducial volume mass,  $N_A = 6.022 \times 10^{23}/\text{mol}$  to the Avogadro number,  $m_{\text{mol},i}$  to the molar mass of the  $i^{\text{th}}$  isotope and  $X_i$  to its relative abundance. Lower and upper integration limits are given by  $E_\nu^{\text{min}} = \sqrt{E_r m_N}/2$  and  $E_\nu = m_\mu/2$ , respectively. Assuming uniform bin size  $\Delta E_r$ , the total event rate evaluated in the  $k^{\text{th}}$  bin central value  $E_r^k$  follows from integration, namely

$$N = \int_{E_r^k - \Delta E_r/2}^{E_r^k + \Delta E_r/2} \frac{dR}{dE_r} dE_r. \quad (33)$$

With the results from Secs. II and III, along with those discussed in this section, we are now in a position to study the precision with which the point-neutron distribution rms can be extracted from data under different weak-charge form factor approaches. For that aim we consider a one-tonne LAr detector as we now discuss.

## V. EXTRACTION OF THE ARGON NEUTRON DISTRIBUTION ROOT-MEAN-SQUARE RADIUS USING DIFFERENT APPROACHES

We now proceed with the determination of the neutron distribution rms radius in some of the different approaches we have discussed. We focus on three cases: **(i)** The weak-charge form factor parametrized à la Helm (for definitiveness), **(ii)** the weak-charge form factor written as in Eq. (17) with the elastic vector form factors parametrized as well à la Helm, **(iii)** model-independent approach based on expansions in terms of even-moments as discussed in Sec. III C. Note that any beyond-the-SM physics effect will diminish the precision with which the neutron distribution rms radius can be extracted. In the following analyses, therefore, those effects are ignored.

Rather than using existing CsI and LAr data [1–3] we instead assume a one-tonne LAr detector with specifications as explained in Sec. IV. This choice provides flexibility with background and so enable us to highlight the main differences arising in each case. As we have already stressed plans for deploying an  $O(\text{tonne})$ -scale LAr detector at the STS [28] have been discussed in Ref. [29].

To proceed we define a simplistic spectral least-square function that accounts only for energy spectral data, but encapsulates the main features of such an experimental environment: Uncertainties from quenching factor, neutrino flux and efficiency as well as Beam Related Neutron (BRN) and Steady State (SS) backgrounds. We, however, do not consider systematic uncertainties due to energy calibration and pulse-shape discrimination and assume that the neutrino-induced neutron (NIN) background is subdominant compared with the BRN and SS backgrounds. Note that such assumptions do not aim whatsoever at representing the actual experimental setup, they are just choices that enable pointing out the effects we are aiming at. The spectral least-square function then reads

$$\chi^2 = \sum_{i=1}^5 \left[ \frac{N_i^{\text{Exp}} - (1 + \alpha) N_i^{\text{Th}}(\mathcal{P})}{\sigma_i} \right]^2 + \left( \frac{\alpha}{\sigma_\alpha} \right)^2. \quad (34)$$

Here  $N_i^{\text{Exp}}$  refers to the number of events in the  $i^{\text{th}}$  bin generated in a toy experiment and  $\alpha$  a nuisance parameter. The least-square function becomes a function of  $\alpha$ , with its actual value following from minimization over it.  $N_i^{\text{Th}}$  the number of events generated by varying the set  $\mathcal{P} = \{R_n^2, \langle R_n^4 \rangle\}$  over a certain range, where  $\langle R_n^4 \rangle$  is only present in case **(ii)**. For the statistical uncertainty we assume  $\sigma_i^2 = N_i^{\text{Th}} + \sum_j B_j$ , with  $\sum_j B_j$  the BRN and SS related backgrounds which we assume to follow the same energy dependence of the signal. The latter assumption is certainly not the case as can be seen in the LAr CEvNS measurement release [3]. However, rather than extrapolating that background to the case we are interested in (multi-ton LAr detector) we believe this assumption represents a better choice. At present  $\text{BR}_{\text{CEvNS}} \simeq 3\%$  while  $\text{BR}_{\text{BRN}} \simeq 14\%$  and  $\text{BR}_{\text{SS}} \simeq 83\%$ , but reduction of that background to lower levels seems achievable in the future [57].

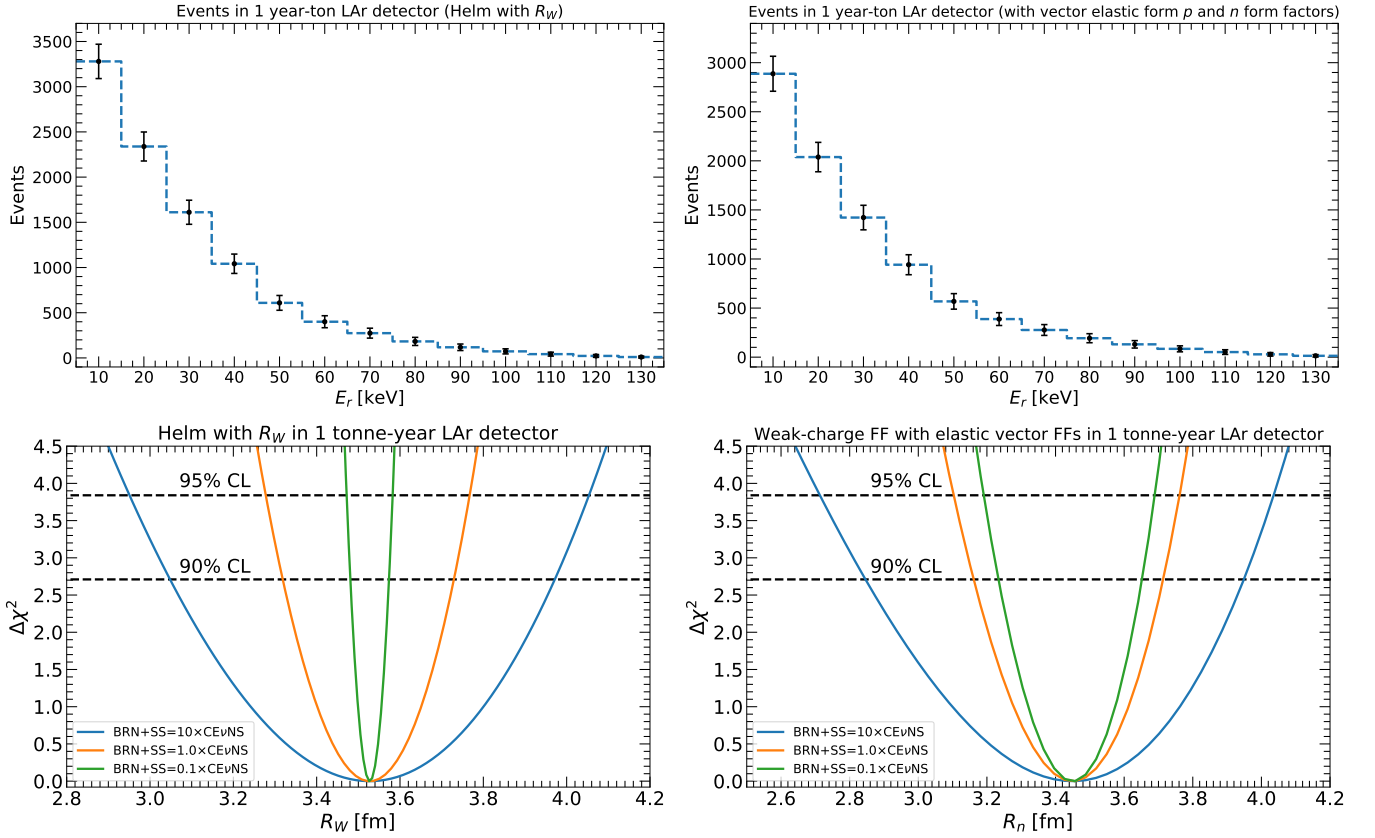


FIG. 6. **Top graphs:** Toy experiment signals calculated by: (i) Using the Helm form factor and fixing the diffraction radius with  $R_W$  (left graph), (ii) Using the weak-charge form factor as given in Eq. (17) (right graph). In both cases  $R_n = R_p + 0.1$  fm, with  $R_p$  calculated from the nuclear charge radius taken from Ref. [48] and Eq. (12). **Bottom graphs:** Least-square function as a function of the weak-charge radius  $R_W$  (left graph) and the point-neutron distribution rms radius (right graph). In both graphs results for two additional analyses with two different BRN and SS background hypotheses are shown as well.

We then assume  $B_j = 10 \times N_j^{\text{Exp}}$ .<sup>7</sup> For the systematical uncertainty encoded in  $\sigma_\alpha$  we take  $\sigma_\alpha = 0.11$  from a 10% uncertainty due to neutrino flux, 5% uncertainty due to efficiency and 1% due to quenching factor. For the efficiency, and following once again the CENNS-10 LAr detector, we assume a Heaviside function at  $5\text{keV}_{\text{nr}}$  and a  $10\text{keV}_{\text{nr}}$  bin size. To generate the toy experiment data, we fix the point-proton distribution rms radius with the aid of Eq. (12) with the values for the different quantities given in Tab. I. For the point-neutron distribution rms radius we use  $R_n = R_p + 0.1$  fm, as we have done in the previous Sections.

Results for cases (i) and (ii) are shown in Fig. 6. Top graphs display results for the toy experiments, while those at the bottom the results of the  $\chi^2$  analyses. Case (i) leads to a fit for  $R_W$  from which we find at the 90% CL the following result

$$R_W = 3.522^{+0.449}_{-0.474} \text{ fm} . \quad (35)$$

The point-neutron distribution rms radius can then be extracted from this result with the aid of Eq. (16). To do so

one should—in principle—take into account uncertainties on the single-nucleon electromagnetic mean-square radii as well as on the  $^{40}\text{Ar}$  nuclear charge radius. These uncertainties are given by  $\Delta\sqrt{r_p^2} = 4.0 \times 10^{-4}$  fm,  $\Delta r_n^2 = 1.7 \times 10^{-3}$  fm<sup>2</sup> [47] and  $\Delta R_C = 1.8 \times 10^{-2}$  fm [48] and so can be safely neglected when compared with those from  $R_W$  in Eq. (35). Results for  $R_n$  at the 90% CL thus read

$$R_n = 3.428^{+0.434}_{-0.458} \text{ fm} . \quad (36)$$

In case (ii), *c'est-à-dire* using Eq. (17) for the weak-charge form factor, allows fitting  $R_n$  directly. In this case the diffraction radius in the proton and neutron elastic vector form factors are fixed from  $R_p$  and  $R_n$ . The former fixed from the nuclear-charge radius and Eq. (12) (using central values for the relevant quantities), while the latter varying over the range [2.6, 4.1] fm. At the 90% CL we find

$$R_n = 3.457^{+0.492}_{-0.611} \text{ fm} . \quad (37)$$

Since the systematic uncertainty as well as the BRN and SS backgrounds for both analyses have been equally fixed and the toy experiments signals have been generated under the assumptions that define each case, differences in the results in

<sup>7</sup> Note that at present BRN plus SS backgrounds in the LAr data release amount to about 29 times the CEvNS signal [3].

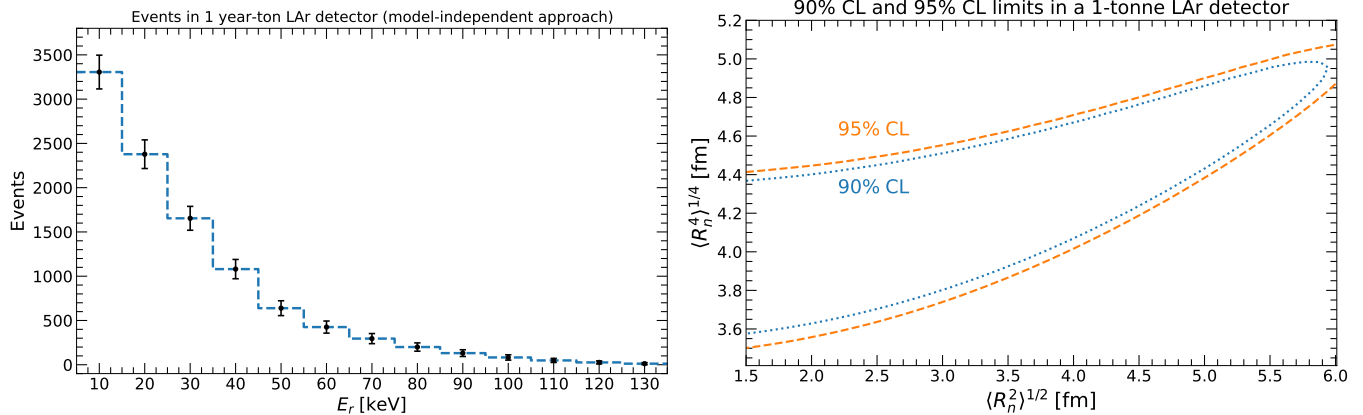


FIG. 7. **Left graph:** Toy experiment data used in the model-independent analysis generated by fixing  $R_n = R_p + 0.1$  fm and  $\langle R_n^4 \rangle = 210.3$  fm<sup>4</sup>, the latter obtained from the results in Eq. (28) in the Helm parametrization case. **Right graph:** 90% and 95% CL isocontours in the neutron distribution rms radius,  $R_n = \sqrt{\langle R_n^2 \rangle}$ , and fourth moment,  $\sqrt{\langle R_n^4 \rangle}$ , plane.

Eqs. (36) and (37) can be only attributed to theoretical assumptions. Parametrizing the weak-charge form factor à la Helm,  $R_n$  can be determined with a  $\sim 14\%$  precision. Using Eq. (17)—including nucleon form factor terms up to order  $Q^2$ —allows a determination at the 18% level. We then conclude that both procedures seem to produce results with comparable levels of precision, though with a slight improvement if a parametrization of the weak-charge form factor is used<sup>8</sup>. In Sec. III we found that numerical deviations from one procedure or the other could be as large as  $\sim 5\%$  in the relevant transferred momentum range. We attribute the differences found here in the extraction of  $R_n$  to that fact.

There is of course the question of whether precision can be improved by improving upon the BRN and SS backgrounds. To assess that question we have run to extra analyses, assuming  $B_j = 1.0 \times N_j^{\text{Exp}}$  and  $B_j = 0.1 \times N_j^{\text{Exp}}$ . The results can be seen in both graphs in Fig. 6. In the case in which the Helm parametrization is used for the weak-charge form factor, precision in the extraction of  $R_n$  improves at the 5% and 1% levels, respectively. In the case in which  $F_W$  is decomposed in terms of elastic vector proton and neutron form factors, instead, at the 8% and 5% levels.

One might wonder whether this conclusion holds as well for heavy nuclei. Although we have not done an analysis for such a case (e.g. for cesium), we find no reason why this should not be the case. Of course nuclear parameters will change, but given the discussion in the previous Sections we expect the trend to be valid in this case too.

<sup>8</sup> Note that in the procedure based on expansion (17) the elastic vector proton and neutron form factors have been as well parametrized using the Helm prescription. Thus this analysis is not a comparison among form factor parametrizations, but rather a comparison between results derived using a parametrization for  $F_W$  (Helm, for definitiveness) and an expansion for  $F_W$ . Implications of different parametrizations (Helm, Klein-Nystrand and symmetrized Fermi function) on the CEVNS event rate have been analyzed in Ref. [36]

We now turn to case (iii), for which for the calculation we do not include nucleon form factors corrections in Eq. (17) and expand the elastic vector proton and neutron form factors in terms of even moments up to order  $Q^4$  (as required from the discussion in Sec. III C). Such procedure leads to

$$F_W = \frac{1}{Q_W} \left[ Zg_V^p \left( 1 - \frac{Q^2}{3!} R_p^2 + \frac{Q^4}{5!} \langle R_p^4 \rangle \right) + Ng_V^n \left( 1 - \frac{Q^2}{3!} R_n^2 + \frac{Q^4}{5!} \langle R_n^4 \rangle \right) \right]. \quad (38)$$

This expression depends—in principle—upon three free parameters: The point-neutron distribution mean-square radius and the proton and neutron fourth moments. However, the contribution controlled by  $\langle R_p^4 \rangle$  can be safely neglected. This can be readily checked by sticking—for this matter—to the Helm parametrization, using then the corresponding expression in Eq. (28) and evaluating the proton  $Q^4$ -to- $Q^2$  ratio. Doing so one finds  $2 \times 10^{-5} (Q/\text{MeV})^2$ , which combined with the fact that  $Q \lesssim 50$  MeV and that the cross section is dominated by the neutron contribution reduces the calculation to a two-parameter problem.

Dropping the proton fourth moment one can then determine from data the neutron distribution mean-square radius and its fourth moment. To generate the toy experiment data we fix  $\langle R_n^4 \rangle$  with the aid of Eq. (28) assuming the Helm parametrization. Results for that pseudo-data are displayed in the left graph in Fig. 7. We then proceed with the least-square analysis by varying  $R_n \equiv \sqrt{\langle R_n^2 \rangle}$  and  $\langle R_n^4 \rangle$ . Results of this calculation in the  $\sqrt{\langle R_n^2 \rangle}$ - $\langle R_n^4 \rangle^{1/4}$  plane are shown in the right graph in Fig. 7. One can see that under the same background and detector assumptions that those used in the previous two cases, only an upper limit on  $R_n$  can be derived. At the 90%CL one gets

$$R_n \lesssim 5.9 \text{ fm}. \quad (39)$$

The result for the fourth moment is instead constrained to an interval (at both the 90% and 95% CLs), although wide.

Fitting  $R_n$  through the model-independent approach has—of course—the advantage of not relying on particular nuclear physics assumptions, but implies fitting two parameters rather than one. That is why, with the statistics and background assumptions we have adopted, only an upper limit on  $R_n$  can be placed.

In some respect this result differs from the one reported in Ref. [38], in particular in the shape of the available 90% and 95% CLs contours. It seems to us these differences are expected because of the following reasons: (a) Our analysis includes the proton contribution (which might become important in regions of parameter space where  $R_n/\langle R_n^4 \rangle^{1/2} \simeq Q/\sqrt{20}$ ), (b) our analysis involves a 3.5 less statistics (a 1-tonne rather than 3.5-tonne LAr detector), (c) our systematic and statistical uncertainties are much larger (in particular the statistical uncertainty which includes a background hypothesis that exceeds the signal by a factor 10), (d) the statistical methods employed in the extraction of the relevant quantities.

Results from the three different approaches we have employed here thus seem to favor the inclusion of nucleon form factors  $Q$ -dependent terms and the decomposition of the weak-charge form factor in terms of elastic vector proton and neutron form factors, as given in Eq. (17). With such an approach a percent determination of the neutron distribution rms radius seems achievable, as shown in Eq. (37). Improving the statistical uncertainty by improving upon BRN and SS backgrounds may lead to  $\sim 1\%$  determination of  $R_n$ .

## VI. CONCLUSIONS

We have quantified uncertainties on the extraction of point-neutron distributions mean-square radii from CEvNS data. Our analysis is motivated by future  $O(\text{tonne})$ -scale CEvNS detectors which will deliver thousands of events per year with well-controlled systematic and statistical uncertainties. Theoretically, uncertainties are encoded in the weak-charge form factor, for which a variety of effects and parametrization approaches have different impact.

Here we have quantified at the weak-charge form factor level uncertainties due to: (i) The absence/presence of single-nucleon electromagnetic mean-square radii in the determination of the point-proton distribution mean-square radius, (ii)  $Q$ -dependent nucleon form factor terms up to order  $Q^2$ , (iii)

parametrizations of the elastic vector proton and neutron form factors, (iv) parametrizations of the weak-charge form factor, (v) model-independent series expansions of the elastic vector proton and neutron form factors.

At the weak-charge level we have found that the inclusion of single-nucleon electromagnetic mean-square radii in the determination of the point-proton distribution mean-square radius has a per mille impact. Thus showing that taking the point-proton distribution mean-square radius equal to the nuclear charge radius is precise enough. Inclusion of nucleon form factors  $Q$ -dependent terms, instead, has a percent effect. Comparison of results from decompositions of the weak-charge form factor in terms of elastic vector proton and neutron form factors with weak-charge form factor parametrizations shows a wider uncertainty, that can rise up to the order of  $\sim 5\%$  ( $\sim 10\%$ ) in the relevant transferred momentum range for light (heavy) nuclei. Comparison of results from decompositions of the weak-charge form factor in terms of elastic vector proton and neutron form factors with series expansions of the elastic vector proton and neutron form factors shows uncertainties of the same order.

To better understand the impact of these effects we have considered pseudo-data from a one-tonne LAr detector with substantial BRN and SS backgrounds, though suppressed compared with those in current LAr data. Our results show that weak-charge form factor parametrizations and decompositions of the weak-charge form factor in terms of elastic vector proton and neutron form factors lead to the same level of accuracy. An indication that under the experimental conditions the analysis has been carried out, both approaches lead to indistinguishable results. Suppressed BRN and SS backgrounds seem to enable reaching  $\sim 1\%$  accuracies in the extraction of  $R_n$ .

## ACKNOWLEDGMENTS

The author warmly thank Dimitrios Papoulias and Jorge Piekarewicz for very useful comments on the manuscript. He thank as well the “Universidad de Antioquia” Physics Department for its hospitality during the completion of this work and ANID for financial support through grant “Fondecyt Regular” 1221445.

- 
- [1] D. Akimov et al. (COHERENT), *Science* (2017), 1708.01294.
  - [2] D. Akimov et al. (COHERENT), *Phys. Rev. Lett.* **129**, 081801 (2022), 2110.07730.
  - [3] D. Akimov et al. (COHERENT) (2020), 2006.12659.
  - [4] M. Cadeddu, C. Giunti, Y. F. Li, and Y. Y. Zhang, *Phys. Rev. Lett.* **120**, 072501 (2018), 1710.02730.
  - [5] D. K. Papoulias, *Phys. Rev. D* **102**, 113004 (2020), 1907.11644.
  - [6] O. Miranda, D. Papoulias, G. Sanchez Garcia, O. Sanders, M. Tórtola, and J. Valle, *JHEP* **05**, 130 (2020), 2003.12050.
  - [7] M. Cadeddu, N. Cargioli, F. Dordei, C. Giunti, Y. F. Li, E. Picciau, C. A. Ternes, and Y. Y. Zhang, *Phys. Rev. C* **104**, 065502 (2021), 2102.06153.
  - [8] P. Coloma, I. Esteban, M. C. Gonzalez-Garcia, and J. Menendez, *JHEP* **08**, 030 (2020), 2006.08624.
  - [9] V. De Romeri, O. G. Miranda, D. K. Papoulias, G. Sanchez Garcia, M. Tórtola, and J. W. F. Valle (2022), 2211.11905.
  - [10] D. K. Papoulias and T. S. Kosmas, *Phys. Rev. D* **97**, 033003 (2018), 1711.09773.
  - [11] J. Liao and D. Marfatia, *Phys. Lett.* **B775**, 54 (2017), 1708.04255.
  - [12] D. Aristizabal Sierra, V. De Romeri, and N. Rojas, *Phys. Rev.* **D98**, 075018 (2018), 1806.07424.

- [13] D. Aristizabal Sierra, V. De Romeri, and N. Rojas, *JHEP* **09**, 069 (2019), 1906.01156.
- [14] D. Aristizabal Sierra, B. Dutta, S. Liao, and L. E. Strigari, *JHEP* **12**, 124 (2019), 1910.12437.
- [15] B. Dutta, S. Liao, S. Sinha, and L. E. Strigari, *Phys. Rev. Lett.* **123**, 061801 (2019), 1903.10666.
- [16] M. Cadeddu, N. Cargioli, F. Dordei, C. Giunti, Y. F. Li, E. Picciau, and Y. Y. Zhang, *JHEP* **01**, 116 (2021), 2008.05022.
- [17] H. Banerjee, B. Dutta, and S. Roy, *Phys. Rev. D* **104**, 015015 (2021), 2103.10196.
- [18] M. Abdullah, J. B. Dent, B. Dutta, G. L. Kane, S. Liao, and L. E. Strigari, *Phys. Rev. D* **98**, 015005 (2018), 1803.01224.
- [19] I. M. Shoemaker, *Phys. Rev.* **D95**, 115028 (2017), 1703.05774.
- [20] S.-F. Ge and I. M. Shoemaker (2017), 1710.10889.
- [21] P. B. Denton, Y. Farzan, and I. M. Shoemaker, *JHEP* **07**, 037 (2018), 1804.03660.
- [22] P. B. Denton and J. Gehrlein, *JHEP* **04**, 266 (2021), 2008.06062.
- [23] P. Coloma, M. C. Gonzalez-Garcia, M. Maltoni, and T. Schwetz (2017), 1708.02899.
- [24] P. Coloma, I. Esteban, M. C. Gonzalez-Garcia, and M. Maltoni (2019), 1911.09109.
- [25] M. Cadeddu, C. Giunti, K. A. Kouzakov, Y.-F. Li, Y.-Y. Zhang, and A. I. Studenikin, *Phys. Rev. D* **98**, 113010 (2018), [Erratum: *Phys.Rev.D* 101, 059902 (2020)], 1810.05606.
- [26] O. G. Miranda, D. K. Papoulias, M. Tórtola, and J. W. F. Valle, *JHEP* **07**, 103 (2019), 1905.03750.
- [27] A. N. Khan, *Nucl. Phys. B* **986**, 116064 (2023), 2201.10578.
- [28] D. Anderson et al., *Technical Design Report Second Target Station*, [https://neutrons.ornl.gov/sites/default/files/SNS\\_STS\\_Technical\\_Design\\_Report\\_2015-01.pdf](https://neutrons.ornl.gov/sites/default/files/SNS_STS_Technical_Design_Report_2015-01.pdf) (2015).
- [29] J. Asaadi et al., in *2022 Snowmass Summer Study* (2022), 2209.02883.
- [30] D. Akimov et al. (COHERENT), *Phys. Rev. D* **102**, 052007 (2020), 1911.06422.
- [31] *Coherent Captain-Mills (CCM) Experiment*, <https://p25ext.lanl.gov/~lee/CaptainMills/> (2018).
- [32] A. A. Aguilar-Arevalo et al. (CCM), *Phys. Rev. D* **106**, 012001 (2022), 2105.14020.
- [33] A. A. Aguilar-Arevalo et al. (CCM), *Phys. Rev. Lett.* **129**, 021801 (2022), 2109.14146.
- [34] O. Tomalak, P. Machado, V. Pandey, and R. Plestid, *JHEP* **02**, 097 (2021), 2011.05960.
- [35] D. K. Papoulias and T. S. Kosmas, *Phys. Rev.* **D97**, 033003 (2018), 1711.09773.
- [36] D. Aristizabal Sierra, J. Liao, and D. Marfatia, *JHEP* **06**, 141 (2019), 1902.07398.
- [37] D. Aristizabal Sierra, B. Dutta, D. Kim, D. Snowden-Ifft, and L. E. Strigari, *Phys. Rev. D* **104**, 033004 (2021), 2103.10857.
- [38] K. Patton, J. Engel, G. C. McLaughlin, and N. Schunck, *Phys. Rev. C* **86**, 024612 (2012), 1207.0693.
- [39] J. L. Friar, J. Martorell, and D. W. L. Sprung, *Phys. Rev. A* **56**, 4579 (1997), nucl-th/9707016.
- [40] C. J. Horowitz and J. Piekarewicz, *Phys. Rev. C* **86**, 045503 (2012), 1208.2249.
- [41] F. J. Ernst, R. G. Sachs, and K. C. Wali, *Phys. Rev.* **119**, 1105 (1960).
- [42] J. Liu, R. D. McKeown, and M. J. Ramsey-Musolf, *Phys. Rev. C* **76**, 025202 (2007), 0706.0226.
- [43] R. S. Sufian, Y.-B. Yang, A. Alexandru, T. Draper, J. Liang, and K.-F. Liu, *Phys. Rev. Lett.* **118**, 042001 (2017), 1606.07075.
- [44] R. H. Helm, *Phys. Rev.* **104**, 1466 (1956).
- [45] S. Klein and J. Nystrand, *Phys. Rev.* **C60**, 014903 (1999), hep-ph/9902259.
- [46] J. D. Lewin and P. F. Smith, *Astropart. Phys.* **6**, 87 (1996).
- [47] P. A. Zyla et al. (Particle Data Group), *PTEP* **2020**, 083C01 (2020).
- [48] I. Angeli and K. P. Marinova, *Atom. Data Nucl. Data Tabl.* **99**, 69 (2013).
- [49] J. Piekarewicz, A. R. Linero, P. Giuliani, and E. Chicken, *Phys. Rev. C* **94**, 034316 (2016), 1604.07799.
- [50] D. K. Papoulias, T. S. Kosmas, R. Sahu, V. K. B. Kota, and M. Hota, *Phys. Lett. B* **800**, 135133 (2020), 1903.03722.
- [51] L. Stodolsky, *Phys. Rev.* **144**, 1145 (1966).
- [52] D. Z. Freedman, *Phys. Rev.* **D9**, 1389 (1974).
- [53] V. B. Kopeliovich and L. L. Frankfurt, *JETP Lett.* **19**, 145 (1974).
- [54] D. Z. Freedman, D. N. Schramm, and D. L. Tubbs, *Ann. Rev. Nucl. Part. Sci.* **27**, 167 (1977).
- [55] M. Hoferichter, J. Menéndez, and A. Schwenk, *Phys. Rev. D* **102**, 074018 (2020), 2007.08529.
- [56] D. Aristizabal Sierra, J. L. Barrow, B. Dutta, D. Kim, L. Strigari, D. Snowden-Ifft, and M. H. Wood (vBDX-DRIFT), *Phys. Rev. D* **107**, 013003 (2023), 2210.08612.
- [57] D. Akimov et al. (COHERENT) (2018), 1803.09183.